Article

Spontaneous Formation of Micelles and Vesicles in Langmuir Monolayers of Heneicosanoic Acid

Martha I. Escamilla-Ruiz, Moises G. Zarzoza-Medina, Maricarmen Ríos-Ramírez, Pablo L. Hernández-Adame,* and Jaime Ruiz-García*

Cite This: ACS Omega 2025, 10, 4224−4232

Read Online

ACCESS | Metrics & More | Article Recommendations | Supporting Information

ABSTRACT: In Langmuir monolayers of heneicosanoic acid ($C_{21}H_{42}O_2$), at low temperature, in the L'_2 and CS crystalline phases, a blinking phenomenon occurs at the same positions of the monolayer, which is called localized oscillations (LO), but its origin has not been clarified. In this study, the LO phenomenon was correlated with the ejection of material out of the monolayer which was analyzed to understand this phenomenon. The techniques used for this purpose were pressure−area isotherms on a Langmuir balance and simultaneous observation of the monolayer by Brewster angle microscopy (BAM). Subsequently, using the Langmuir−Blodgett technique, the monolayers were transferred using freshly cleaved mica substrates for analysis by atomic force microscopy (AFM). Our results showed that the origin of the LO is related to a spontaneous formation of micelles and vesicles, since in AFM images these structures were observed in a size range from 4 to 16 nm. In addition, the AFM images showed that the difference between the heights of the L'_2 and CS crystalline phases ranges from 13 to 15 Å.
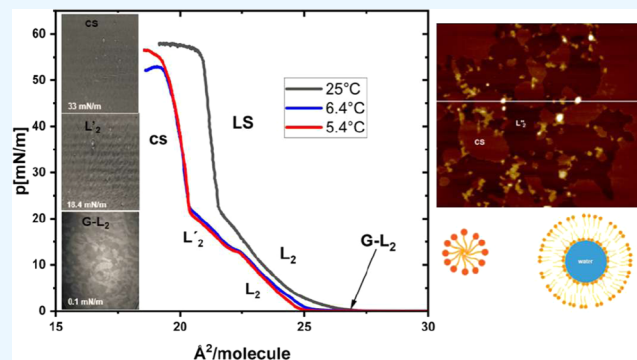
1. INTRODUCTION

Fatty acids (FAs) are amphiphilic molecules that consist of a carboxylic acid group and a saturated hydrocarbon chain or with different degrees of unsaturation.[1] They are the building blocks of various lipids such as phospholipids and sphingolipids.[2−4] These lipids in turn, form part of the structure of cell membranes and regulate diverse biochemical processes in cells,[5] in particular, lipids have an essential role in the structure and function of the brain; they constitute around 50% of its dry weight.[6] Polyunsaturated fatty acids (PUFAs) such as arachidonic acid (AA, 20:4n-6) and docosahexaenoic acid (DHA, 22:6n-3) are the primary fatty acids that compose the central nervous system, they participate in the regulation of membrane fluidity, neuronal communication through synaptic vesicles, axonal growth, memory, and the anti-inflammatory response in many diseases.[7−9] On the other hand, saturated fatty acids (SFAs) are known to reduce the elasticity of nerve cells[10] they have been associated with coronary heart disease, inflammatory diseases and Alzheimer's disease.[11−14] Most of the studies on SFAs have been carried out on even-chain fatty acids because they have a high concentration in human plasma; however, their counterpart (odd-chain SFAs or OCFAs) has been less studied because their concentrations were thought to be negligible in humans. For this reason, OCFAs have mainly been used as biomarkers for dietary analysis and for some diseases.[15] Recently, OCFAs have been gaining ground in

research, as several studies have shown that dietary intake of OCFAs has a beneficial effect on reducing the risk of coronary heart disease, type 2 diabetes, Alzheimer's disease, and anemia, among other diseases.[16,17] OCFAs are present in low concentrations in dairy products, some fish and plants. In a study conducted by Wei et al.,[18] they reported for the first time the presence of various OCFAs such as tridecanoic, pentadecanoic, heptadecanoic, trichosanoic and heneicosanoic acids, in coix seeds, which are widely used in Asian medicine for their therapeutic effects in clinical cancer treatments.[19,20] Ruminant-derived products are the main source of OCFAs in the human diet,[21] several studies have shown that the lipid profile in milk is dependent on the diet ingested by the ruminant animals; for example, supplementation with fish oils and microalgae increases the concentrations of OCFAs in the cow's milk.[22] Heneicosanoic Acid (C21) is an OCFA present in low concentrations in breast milk,[23] fish,[24] seeds[18] and as the composition of cerebroside, a type of glycosphingolipid that is found in the cell membranes of the nervous system.[25]

The study of C21 can be used as a reference for the understanding of cellular processes because of its ability to form micelles and vesicles under certain conditions. It is well-known that chemical neurotransmission is mediated by the exocytosis of neurotransmitters stored in vesicles known as synaptic vesicles.[7] The acid C21 was previously reported to exhibit a peculiar phenomenon known as localized oscillations (LO) in the L'_2 and CS crystalline phases in Langmuir monolayers by Galvan et al.[26] and Ramos and Castillo.[27] The authors suggest that this phenomenon may be related to a process of matter expulsion or the formation of granules, however, the origin of this phenomenon remains unclear.

In this work experimental data show the formation of micelles and vesicles in L'_2 and CS phases, which could explain the origin of the LO. Brewster Angle Microscopy (BAM) shown a monolayer filled with holes with different diameters and Langmuir−Blodgett and atomic force microscopy (AFM) techniques demonstrate the presence of micelles and vesicles of a variety of sizes.

2. MATERIALS AND METHODS

2.1. Reagents. Heneicosanoic acid (C21:0) was purchased from Sigma-Aldrich Quimica, S.A. de C.V. (99%) was used without any further purification. The spreading solution of the fatty acid was prepared with pure chloroform (HPLC, 99.9%, Sigma-Aldrich) at a concentration of 1 mg/mL. Using a 100 μL Hamilton glass microsyringe, 50 μL of the Heneicosanoic acid solution was spread gently onto the surface of the subphase consisting of mili Q ultrapure water system (>18.3 $M\Omega$ cm^{-1})

2.2. Langmuir−Blodgett Trough. A Langmuir−Blodgett trough (model 611, NIMA Technology Ltd., Coventry, England) was used to measure the pressure−area isotherms, using a filter paper as the Wilhelmy plate for the surface pressure determination (with an accuracy of ±0.1 mN/m). The trough was placed on an antivibratory table and filled with deionized water (bioresearch grade water >18.3 $M\Omega$ cm^{-1} of resistivity, Barnstead/Thermolyne, Dubuque, Iowa). The trough is equipped with two poly(tetrafluoroethylene) (PTFE) barriers fitted with steel bars to provide a symmetric compression and a working area of 700 cm^2. During the experiments, the temperature was controlled at 5.4, 6.4, and 25 °C using a water recirculator bath (Neslab, United States). Before starting each experiment, the subphase and trough cleanliness were tested by closing the barriers and checking that the pressure sensor readings were less than 0.1 mN/m when the Langmuir trough barriers were fully closed (and by the presence of a dark background only, observed by Brewster Angle Microscopy). Using a 50 μL glass microsyringe, the fatty acid C21 solution was gently deposited on the air/water interface and allowed to stand for at least 30 min to allow the chloroform evaporation before starting each experiment. The monolayer was then compressed at 11 cm^2/min. Some monolayers were transferred using freshly cleaved mica substrates with a dipping speed of 1 mm/min and a surface pressure of 15 mN/m with the Langmuir−Blodgett technique.

2.3. Brewster Angle Microscopy. The images of the monolayers, morphologies and phase transitions that characterize the C21 fatty acid were taken using a Brewster Angle Microscope (BAM, Nanofilm EP4, Accurion GmbH, Germany). BAM is based on the study of the intensity of a reflected light beam coming from an interface with a monolayer to be study on a clean subphase illuminated with

a monochromatic and *p*-polarized light beam.[28] The main characteristic of this beam is when the angle of incidence on pure water is at the Brewster angle (53.15°), does not reflect any light beam, therefore, it is used to distinguish between the monolayer to be analyzed, as long as the monolayer has a refractive index different to the subphase.[29]

2.4. Atomic Force Microscopy. For the atomic force microscopy (AFM) observation, the monolayers were transferred using freshly cleaved mica substrates, with an extraction speed of 1 mm/min and a surface pressure of 15 mN/m. The measurements were performed with a MultiMode V8 SPM NanoScope microscope (Bruker, Santa Barbara, CA) in tapping mode at room temperature using a RTESPA silicon cantilever (Bruker, Santa Barbara, CA) with a nominal tip radius <10 nm and a resonance frequency of 300−400 kHz.

2.5. Experimental Process. During the execution of this project, a variety of temperatures were studied to explore the conditions under which the localized oscillations (LO) phenomenon occurs. Each experiment was repeated 3 times for each investigated temperature, allowing us to assess the consistency of the observed phenomenon. However, the data presented within the manuscript specifically correspond to the temperatures where the localized oscillations were detected (5.4 and 6.4 ± 0.5 °C, respectively). Additionally, the temperature of 25 ± 0.5 °C, where the LO phenomenon was not visualized, is reported. The replicates conducted demonstrated a high reproducibility of the results, which confirms the validity of our observations. These were carried out according to Figure S1 of the Supporting Information.

3. RESULTS AND DISCUSSION

3.1. L'_2 and CS Crystalline Phases of Heneicosanoic Acid (C21). C21 presents a great variety of phases despite being a single component as has previously been reported by Ramos and Castillo[27] and Teer et al.[30] in their phase diagram. The nomenclature used for the crystalline phases of C21 is based on the classification previously reported by Kaganer et al.[31] In their work, the liquid-expanded phase is referred to as L_E or L_1, while the condensed phases, which appear at different areas per molecule and temperatures, are called L_2, L'_2, L''_2 or CS. The ranges of values for each phase in our study were taken from the C21 phase diagram proposed by Teer et al.[30] This nomenclature system is widely accepted and has been consistently adopted by other research groups to date.[27,30]

Ramos and co-workers reported the LO in the L''_2 phase, where the molecules are tilted, and in the crystalline CS phase. In our investigation, we found this phenomenon in the L'_2 and the CS phases according to Teer and co-workers. The difference between the L'_2 and the CS is that the molecules of the L'_2 phase are tilted toward their nearest neighbor,[31] while the CS phase has untilted chains. Figure 1 shows three different surface pressure isotherms, where the change in slope is due to phase transitions, and at temperatures of 5.4 and 6.4 °C is where the oscillations are observed, and at 25 °C the oscillations do not appear. Our isotherms agree well according to the C21 phase diagram from Teer group.[30]

The isotherms in Figure 1 show the presence of a coexistence region between the gas (G) and L_2 phases in areas per molecule greater than 24.5 $Å^2$/molecule and at surface pressures close to 0 mN/m. As the lateral pressure of C21 increases, the hydrocarbon chain inclination begins to form the pure L_2 phase only, between pressures of about 0 to 12.5 mN/m. However, at temperatures of 5.4 and 6.4 °C (red
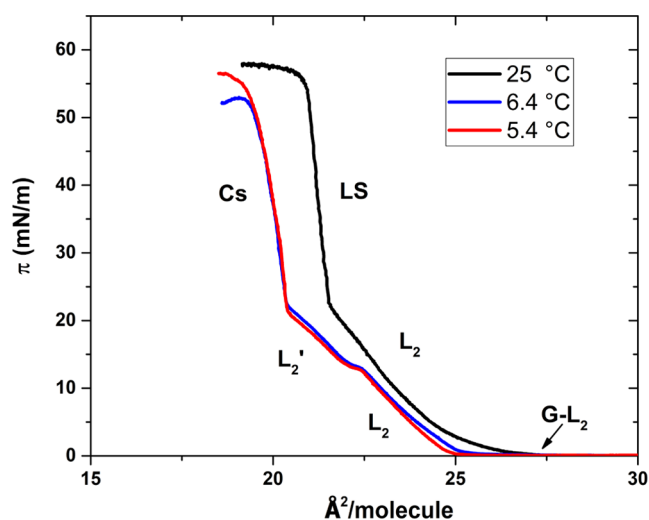
Figure 1. C21 isotherms at three different temperatures conditions showing a variety of phases. The oscillations are observed only at 5.4 and 6.4 °C, while they are not observed at 25 °C.

and blue isotherms in Figure 1, respectively), the crystalline phases L'_2 and CS are observed. The L'_2 phase appears in both isotherms between surface pressures of approximately 12.5 to 22 mN/m. At surface pressures close to 22 mN/m, there is a new phase transition from the L'_2 phase to the CS phase. However, at a temperature of 25 °C (black isotherm in Figure 1), a different phase is observed, namely the LS, and the L_2 is still present.

Figure 2 shows BAM images obtained in the L'_2 and CS phases at both temperatures of 5.4 and 6.4 °C. A homogeneous layer of C21 is observed (Figure 2a), which appears as a dark gray tone, corresponding to the crystalline L'_2 phase. In addition, there are lighter gray tones forming a mosaic of elongated irregular domains which represents the CS phase. The contrast between these two shades is attributed to the variation in the inclination of the C21 hydrocarbon chain within the phase and therefore, each shade of gray corresponds to a different direction of tilt of the hydrocarbon chain.[27] In the same way, black holes and white clusters with a series of rings around them can be observed within the CS crystalline phase. The rings are known as Newton rings and are interference patterns that appear in monolayers as concentric circles alternating between bright and dark.[32] Newton's rings are formed due to a type of multilayer defect and are common in the condensed phases of monolayers.[26,27] When a second compression is performed on the same monolayer (Figure 2b), a network of holes is observed in the C21 monolayer. It is important to mention that in this place (holes) the LO appear and disappear rapidly. This phenomenon is described in the next section. Similarly, in Figure 2a,c,d you can see light and dark horizontal stripes; these are an artifact caused by the optics of the microscope (BAM). However, this is not considered within the monolayer analysis and therefore does not affect the measurements made.
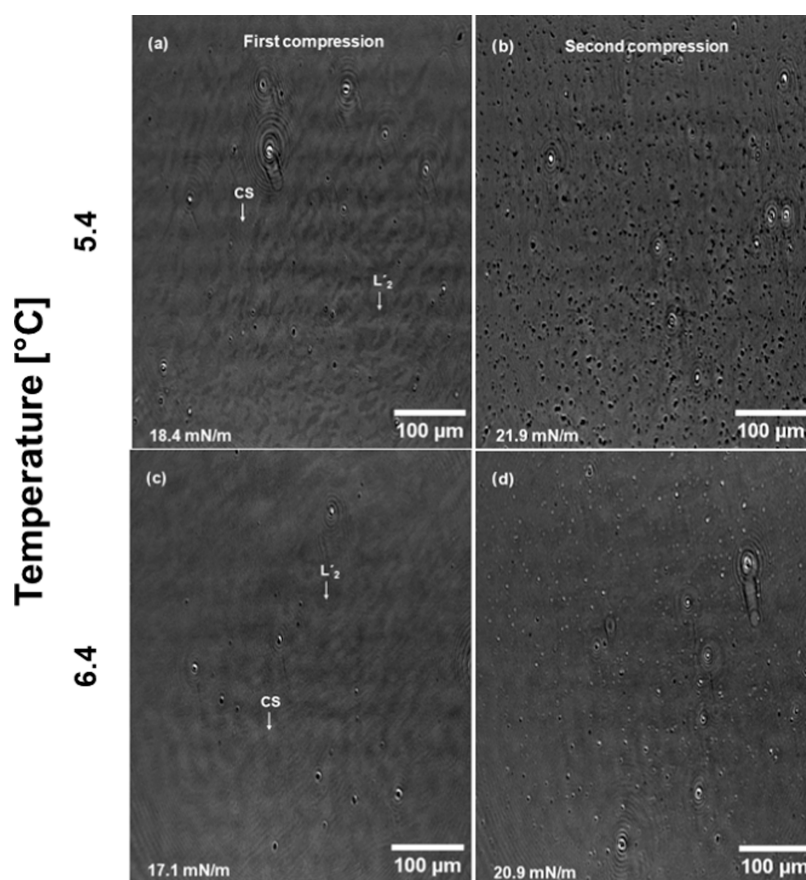

Figure 2. Brewster Angle Microscopy (BAM) images of the L'_2 and CS phases of C21 at low temperatures. (a, b) First and second compressions at 5.4 °C, respectively. (c, d) First and second compressions at 6.4 °C, respectively.
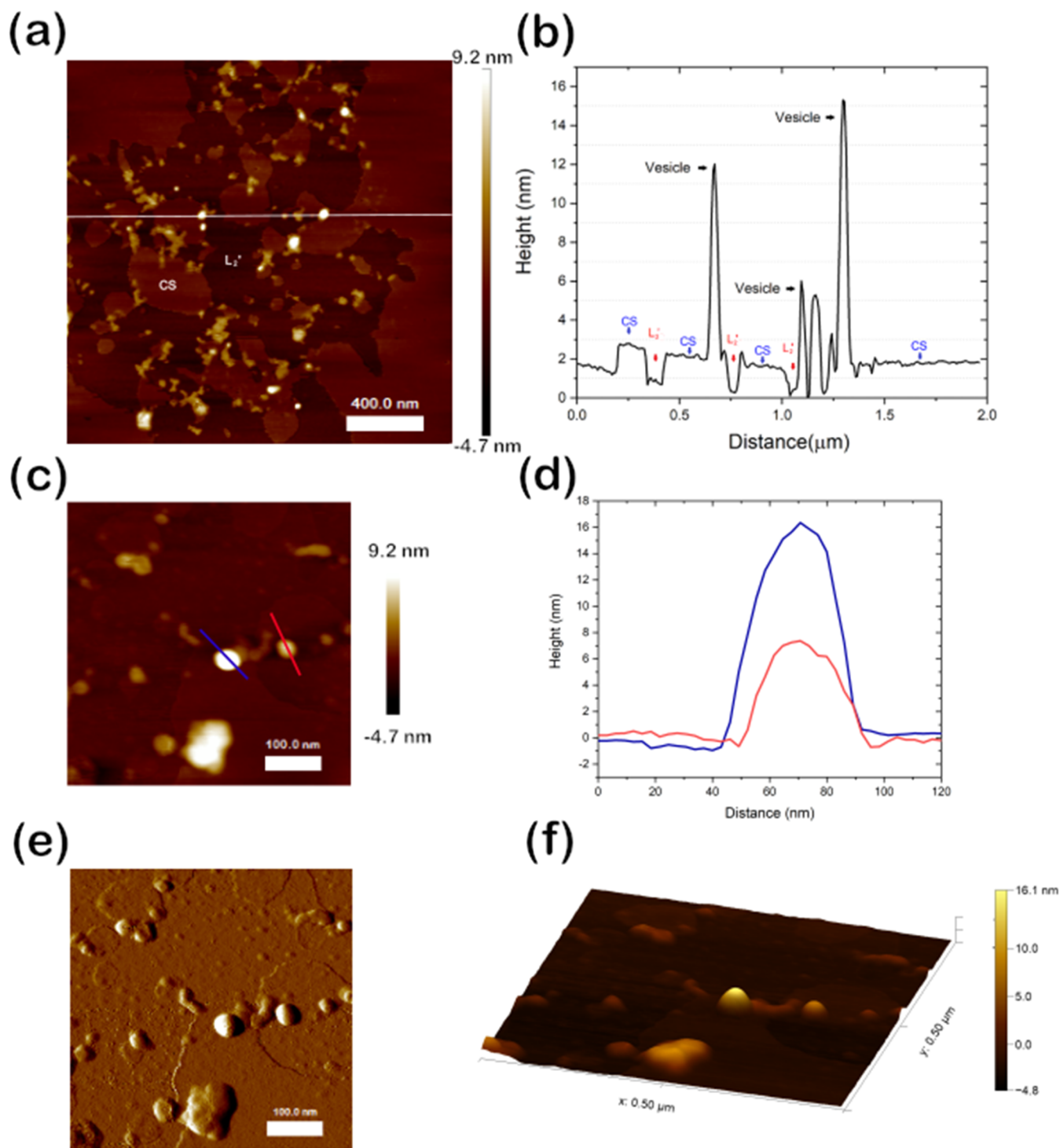
Figure 3. Atomic Force Microscopy images of C21. (a) L'$_2$ and CS coexisting phases at low temperatures together with the micelles and vesicles formation in defect zones of CS phase. (b) Cross-sectional graph to determine the size of the ejected material. (c) Higher resolution AFM height image that provide a better visualization of the spherical structures, (d) the blue and red lines correspond to the height profile of these structures. (e) The amplitude error and (f) the 3D-AFM images allow us to identify vesicles in the sample.

Figure S2 of the Supporting Information shows the BAM images obtained along the isotherms studied and shows the different C21 phases. The BAM images obtained for the 25 °C isotherm did not show the LO phenomenon despite the similarity in the morphology of the lower temperature phase.

3.2. Localized Oscillations (LO). In addition to the structures detailed above for low-temperature isotherms, the LO of C21 could be observed. It has been reported that LO are visible only in the L'$_2$ and CS crystalline phases within a temperature range between 2−6 °C.[27] In this work, it was possible to observe LO around 22 mN/m, and they increased with the compression of the monolayer. According to the isotherms in Figure 1, the LO began upon reaching the CS phase and within the elongated light gray irregular domains shown in Figure 2a. The particularity of the LO is that they appear and disappear rapidly throughout the monolayer and in
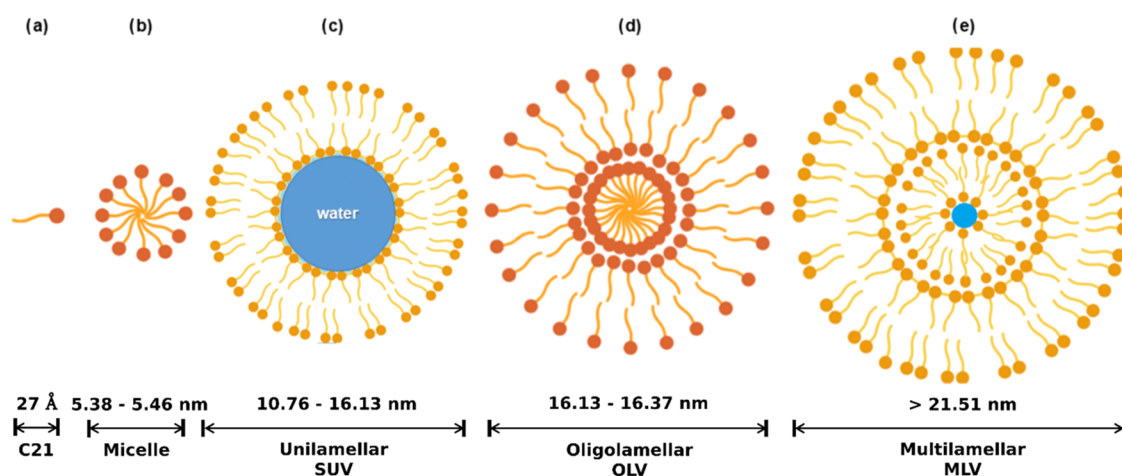
Figure 4. Estimation of micelle and vesicles formation size by Rubber stretching method. (a) Length of C21, (b) micelle size, (c) unilamellar vesicle, (d) oligolamellar vesicle and (e) multilamellar vesicle.

the same position as the clusters and holes described above. In the Supporting Information file, there are several links to some videos acquired in real time and along the isotherms at different temperatures where the LOs were observed. Here we can see that the LO phenomenon is found throughout the monolayer appearing and disappearing at high speed. This phenomenon has been previously studied by the group of Ramos and Castillo,[27] and they conclude that this process is better known as blinking. The authors deduce that the ring patterns observed as LO are airy patterns due to Fraunhofer diffraction produced by the light reflected from the multilayer granules. In addition, they suggest that the LO could be due to a successive process of expulsion of matter, granule formation and discontinuous growth, reusing the expelled material, and giving a possible origin to the blinking. However, the origin of this phenomenon is still unknown. The LO are related to stress and energy in areas of the monolayer with a high concentration of defects. Galvan et al. mention that it is a different way of starting the formation of multilayers, where material is expelled from the monolayer before reaching the collapse pressure.[26] When a second compression is performed on the same monolayer (Figure 2b−d), a network of holes is observed to form in the C21 monolayer. To observe the behavior of the C21 monolayer under pressure changes in the L2′ phase, the surface compressibility modulus (Cs^{1-}) was calculated. The results are presented in Figure S3 of the Supporting Information. This figure shows that in the L_2 phase region at 25 °C, the monolayer compressibility remains stable. However, this behavior changes in the L_2' region at lower temperatures (5.4 and 6.4 °C), where the compressibility modulus exhibits fluctuations and decreasing values. These results suggest unusual behavior of the monolayer, indicating it is in a region of instability or phase transition.[33] In an unstable state, any additional compression can produce the monolayer collapse or its molecules to become disorganized.[34] Compressing the C21 monolayer with the mobile barriers of the Langmuir Trough introduces additional force, causing the monolayer to fluctuate along the surface, promoting the formation of localized oscillations (LO) throughout the monolayer. These oscillations result in the expulsion of material into the subphase, facilitating the formation of micelles and vesicles.

3.3. Morphological Observation of Spherical Structures.

To validate our hypothesis, a series of measurements

using atomic force microscopy (AFM) were performed within the region where LO's were detected. Monolayers of C21 acid were transferred to freshly cleaved mica substrates using the Langmuir−Blodgett technique. This process required bringing the isotherm to its equilibrium pressure while maintaining stability for 2 h. Subsequently, the transfer was carried out ensuring a constant pressure and a transfer speed of 1 mm/min. The transfer occurred at a pressure of 15 mN/m and a temperature of 5.4 °C, ensuring the presence of the L_2' phase. The AFM image (Figure 3) shows morphologies that resemble those observed in the images obtained through BAM.

In Figure 3a, a mosaic pattern consisting of irregular domains in two different shades is observed. The background has a dark brown tone, corresponding to the L'_2 phase, while a lighter brown color represents the crystalline phase CS. It is important to highlight that in the interfacial zone of the CS phase, cumulus with a white spherical shape are also observed. Because of their size, these structures correspond mostly to vesicles formation. The height profile shown in Figure 3b represents the cross-sectional graph (white line of Figure 3a). Here, it is seen that these structures have sizes between 4 and 16 nm. Our deduction of vesicles shapes was determined not only by the size, but also by the morphology observed by the characteristic shown in the height profile, which closely aligns with profiles reported in the visualization of vesicles by AFM measurements.[35,36]

Additionally, in Figure 3c, we also see different structures in our system, but only the ones that show the typical flattened round shape (blue and red lines) were considered for our statistics. The profile curves of the blue and red lines in Figure 3d, show that the diameter of our spherical structures is much larger than the height (6−16 nm), and this is related to the adsorption process to the mica.[37] We can notice with more detail the irregular shapes that are present in our transferred monolayers in Figure 3e,f. We believe that these objects could be due to interactions between vesicles, fusion events, or the presence of multilamellar structures.[38] More details of the analysis carried out by AFM can be found in Figures S4 and S5 of the Supporting Information.

Some research groups have demonstrated the formation of vesicles in phospholipid monolayers. For example, Gopal et al.[39,40] examined a phospholipid mixture of dipalmitoylphosphatidylcholine and palmitoyloleoylphosphatidylglycerol
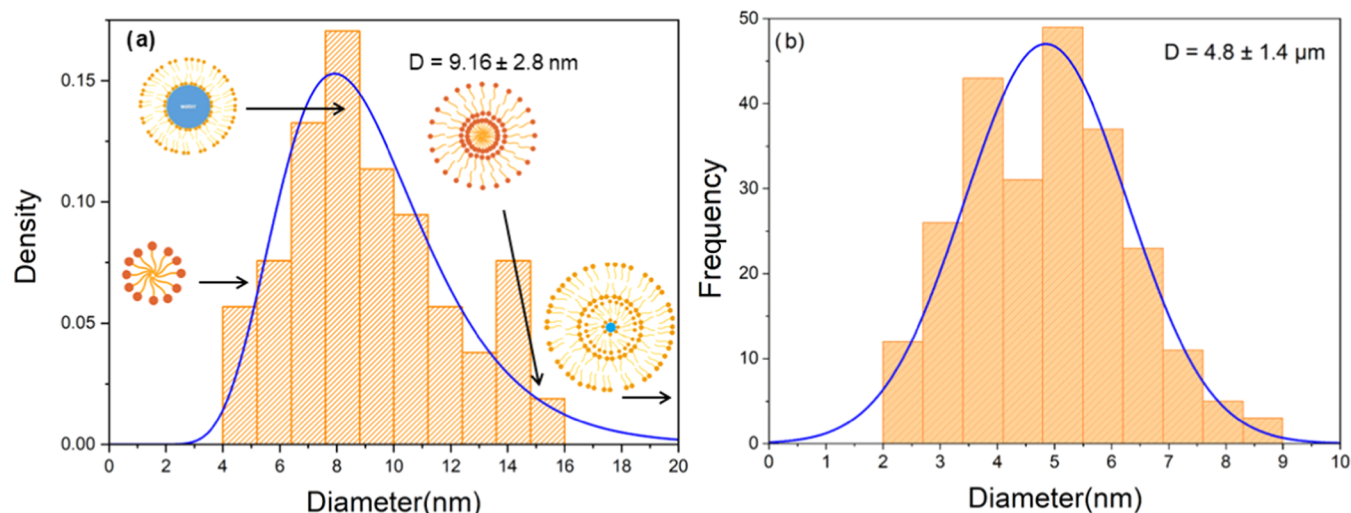
Figure 5. Vesicle size distribution histograms measured by (a) AFM height images (n = 50) and (b) hole size distribution measured by BAM images (n = 120). The blue solid curve corresponds to the log-normal distribution fit.

(DPPC:POPG) using Langmuir monolayers and fluorescence microscopy. In this study, they analyzed how the monolayer collapses over a temperature range of 20 to 40 °C and determined that at temperatures below 28 °C, the monolayer is biphasic and collapses, forming folds. On the other hand, when the temperature is above 33.5 °C, the monolayer becomes homogeneous and collapses, forming micrometer-scale vesicular structures characterized by globular or tubular shapes. In another study by Ridsdale et al.,[41] DPPC films were analyzed at the air-buffer interface. Transmission electron microscopy (TEM) was used to examine the film, revealing the presence of folds on the film's surface as well as the formation of vesicular structures. In another study performed by Hatta,[42] he found vesicle formation in Langmuir monolayers in octadecanoic acid (C18). The experiments were carried out in a pH range of 6 to 8 and analyzed by phase contrast microscopy. Apparently, the formation of the vesicles is due to the presence of defects in the monolayers, where the lipid material start solubilizing into the subphase. For all these reasons, our results show that the LO are a consequence of the formation and expulsion of micelles and vesicles.

At the same time and within Figure 3b, we can also see the height between the L′$_2$ (red arrows) and CS (blue arrows) phases. It is around 13 to 15 Å. Previous studies performed by Chi et al.[43] determined the phases of stearic acid (C18) and observed a height difference of approximately 15 to 20 Å between the liquid-condensed (LC) and liquid-expanded (LE) phases, similar to our results. C21 and C18 share similarities, as both are saturated fatty acids. To distinguish between the height of a monolayer and a vesicle is that the monolayer usually has a plateau-shaped distribution.[44,45]

3.4. Estimation of Micelles and Vesicles Sizes.
To estimate the size distribution of the micelles and vesicles formed by the C21 fatty acid, the stretching Rubber method was used.[46,47] The results are shown in Figure 4, were we used a C21 length of 27 Å.[48] The temperatures and pressures were considered in the range of 5.4 to 6.4 °C and 12.5 to 22 mN/m, respectively.

The estimated diameters for C21 micelles are between 5.38−5.46 nm, as can be seen in Figure 4b. However, due to the spontaneous nature of LO, we can have a variety of sizes in the vesicular formations. If we consider the minimum micelle

size, various vesicles species can be identified. Unilamellar vesicles (Figure 4c) have an estimated diameter of 10.76 to 16.13 nm, while oligolamellar vesicles (Figure 4d) have diameters of 16.13 to 16.37 nm. Additionally, multilamellar vesicles (Figure 4e) have diameters sizes greater than 21.51 nm. These results align perfectly with the vesicle sizes distributions determined through AFM measurements (Figures 3 and 5).

Analysis of the size distribution (Figure 5a) demonstrates the presence of micelles and vesicles with a range of sizes between 4 and 16 nm. By performing a fit with a Gaussian function, we can determine that the average size of the vesicles formed was 9.16 ± 2.8 nm. These vesicular formations fall within the estimation of unilamellar vesicles (Figure 4c) and can be classified as small unilamellar vesicles (SUVs). On the other hand, and within Figure 2b, where black holes were observed in the C21 monolayer by BAM images, it can be seen that the origin of these SUVs comes from the formation of larger vesicles. Analysis of the size distribution of the black holes revealed dimensions between 2 to 8 μm with an average of 4.8 ± 1.4 μm. These sizes correspond to multivesicular vesicles (MVVs). It is known that during the formation of MVVs or MLVs, their size can be reduced to the formation of large and small unilamellar vesicles (LUVs and SUVs, respectively) due to mechanical forces during their formation process, either by extrusion and/or sonication.[49] In our case, the mechanical force generated by the mobile barriers of the Langmuir balance can be considered as the external force to achieve this reduction. In this work we do not discard the possibility of MVVs formation. We believe that this type of vesicles could have been expelled into the subphase, however due to technical difficulties, the subphase could not be analyzed to measure this type of vesicle formations. Nevertheless, in this work we detected and analyzed SUVs that were detached due to this phenomenon and were trapped at the air−water interface.

Langmuir monolayers and liposomes are both utilized as models for biological membranes and explore processes related to them. Langmuir monolayers, which primarily focus on analyzing conformational changes and interactions of membranes with pharmacological substances and biologically relevant materials, also serve as models to understand the

behavior of lipids at the air−water interface. These studies provide crucial insights into the organization and dynamics of lipid bilayers, which constitute the structural basis of liposomes. The latter, on the other hand, stand out for their utility as drug carriers, thanks to their ability to encapsulate both hydrophilic and hydrophobic compounds.[50,51]

The localized oscillations observed in C21 monolayers may be related to the self-assembly and disassembly processes of lipid structures. These processes are fundamental in the controlled release of drugs, where the organization and disorganization of lipid structures can control the release of the active substance. On the other hand, the compressibility modulus of the monolayers and the fluctuations observed in the L'_2 phase at low temperatures suggest a state of instability or phase transition. In drug delivery systems, these phase transitions can be exploited to control drug release in response to changes in the environment, such as pH or temperature.[52,53]

4. CONCLUSIONS

In this work, we carried out experimental approaches to investigate the localized oscillations of heneicosanoic acid within the L'_2 and CS phases. Langmuir monolayer and Brewster angle microscopy (BAM) experiments demonstrated the presence of black holes along the C21 monolayer suggesting the expulsion of material into the subphase. Analysis of the hole size distribution within the monolayer indicates that these formations could be due to the formation of multivesicular vesicles (MVVs) with averages around 4.5 μm. On the other hand, by the Langmuir−Blodgett technique we transferred samples onto mica, and AFM images of the samples were obtained. These images showed the presence of micelles and small unilamellar vesicles (SUVs) trapped at the air−water interface along with the monolayer, ranging in size from 4 to 16 nm. Additionally, AFM analysis reveals that the height between the L'_2 and CS crystalline phases is between 13 to 15 Å. Therefore, we conclude that localized oscillations phenomenon is caused for the formation and expulsion of micelles and vesicles of different sizes.

■ ASSOCIATED CONTENT

Ⓢ Supporting Information

The Supporting Information is available free of charge at https://pubs.acs.org/doi/10.1021/acsomega.4c03100.

> C21 Pressure−area isotherms in the different replicas at the temperatures of (a) 25, (b) 6.4 and (c) 5.4 ± 0.5 °C (Figure S1); BAM images obtained along the C21 isotherms at different temperatures, the scale bar used in column one (low pressures) is similar for all other images (Figure S2); surface compression modulus values (Cs^{1-}) of C21 acid for each of the replicas and temperatures, (a−c) 25 °C, (d−f) 6.4 °C and (g−i) 5.4 °C (Figure S3); AFM morphology analysis: (a) A representative AFM height image of the transfer monolayer of C21, after the image was flattened, we used a height mask with a threshold above 4 nm to differentiate between the L'_2 and CS phases from other structures, (b) we then measured the height of the structures with spherical morphology (green arrows), using (c) amplitude error images to manually discard nonspherical objects and other structures that could be fusion events (blue arrows), we collected the heights of 50 objects with spherical shape from different transferred

> monolayers at a pressure of 15 mN/m and a temperature of 5.4 °C (Figure S4); (a) another representative sample AFM height image to which the same analysis was applied, (b) AFM height image with the mask and the (c) amplitude error image, only the height of the spherical shape structures (green arrows) was considered for our statistics (Figure S5); Brewster angle microscope videos are acquired in real time and the observation range is 462 × 564 μm^2, the video speed is 1× (PDF)

■ AUTHOR INFORMATION

Corresponding Authors

Pablo L. Hernández-Adame − *Laboratorio de Física Biológica, Instituto de Física, Universidad Autónoma de San Luis Potosí, San Luis Potosí 78290, México;* Email: pabloyae_2@hotmail.com

Jaime Ruiz-García − *Laboratorio de Física Biológica, Instituto de Física, Universidad Autónoma de San Luis Potosí, San Luis Potosí 78290, México;* ⓘ orcid.org/0000-0003-3730-3825; Email: jaime@ifisica.uaslp.mx

Authors

Martha I. Escamilla-Ruiz − *Laboratorio de Física Biológica, Instituto de Física, Universidad Autónoma de San Luis Potosí, San Luis Potosí 78290, México*

Moises G. Zarzoza-Medina − *Laboratorio de Física Biológica, Instituto de Física, Universidad Autónoma de San Luis Potosí, San Luis Potosí 78290, México*

Maricarmen Ríos-Ramírez − *Laboratorio de Física Biológica, Instituto de Física, Universidad Autónoma de San Luis Potosí, San Luis Potosí 78290, México*

Complete contact information is available at:
https://pubs.acs.org/10.1021/acsomega.4c03100

Author Contributions

M.I.E.R. and M.G.Z.M. performed the Langmuir balance and BAM experiments. M.R.R. performed the measurements and analysis by AFM. PLHA and JRG were the project managers. All authors participated in editing the manuscript.

Notes

The authors declare no competing financial interest.

■ ACKNOWLEDGMENTS

■ REFERENCES

(1) Lund, J.; Rustan, A. C. Fatty Acids: Structures and Properties. In *Encyclopedia of Life Sciences*; Wiley, 2005; pp 283−292.

(2) De Carvalho, C.; Caramujo, M. J. The Various Roles of Fatty Acids. *Molecules* **2018**, *23*, 2583−2618.

(3) Fagone, P.; Suzanne, J. Membrane phospholipid synthesis and endoplasmic reticulum function. *J. Lipid Res.* **2009**, *50*, S311−S316.

(4) Röhrig, F.; Schulze, A. The multifaceted roles of fatty acid synthesis in cancer. *Nat. Rev. Cancer* **2016**, *16*, 732−749.

(5) Koundouros, N.; Poulogiannis, G. Reprogramming of fatty acid metabolism in cancer. *Br. J. Cancer* **2020**, *122*, 4−22.

(6) Chianese, R.; Coccurello, R.; Viggiano, A.; Scafuro, M.; Fiore, M.; Coppola, G.; Operto, F. F.; Fasano, S.; Laye, S.; Pierantoni, R.;

Meccariello, R. Impact of Dietary Fats on Brain Functions. *Curr. Neuropharmacol.* **2018**, *16*, 1059−1085.

(7) Binotti, B.; Jahn, R.; Pérez-Lara, Á. An overview of the synaptic vesicle lipid composition. *Arch. Biochem. Biophys.* **2021**, *709*, No. 108966.

(8) Chanaday, N. L.; Cousin, M. A.; Milosevic, I.; Watanabe, S.; Morgan, J. R. The Synaptic Vesicle Cycle Revisited: New Insights into the Modes and Mechanisms. *J. Neurosci.* **2019**, *39*, 8209−8216.

(9) Falomir-Lockhart, L. J.; Cavazzutti, G. F.; Giménez, E.; Toscani, A. M. Fatty Acid Signaling Mechanisms in Neural Cells: Fatty Acid Receptors. *Front. Cell. Neurosci.* **2019**, *13*, 162−185.

(10) da Silva-Santi, L. G.; Antunes, M. M.; Mor, M. A.; de Almeida-Souza, C. B.; Visentainer, J. V.; Carbonera, F.; Crisma, A. R.; Masi, L. N.; Hirabara, S. M.; Curi, R.; Bazotte, R. B. Brain Fatty Acid Composition and Inflammation in Mice Fed with High-Carbohydrate Diet or High-Fat Diet. *Nutrients* **2018**, *10*, 1277−1288.

(11) Kris-Etherton, P. M.; Petersen, K.; Horn, L. V. Convincing evidence supports reducing saturated fat to decrease cardiovascular disease risk. *BMJ Nutr., Prev. Health* **2018**, *1*, 23−26.

(12) Gustafson, D. R.; Bäckman, K.; Scarmeas, N.; Stern, Y.; Manly, J.; Mayeux, R.; Gu, Y. Dietary fatty acids and risk of Alzheimer's disease and related dementias: Observations from the Washington Heights-Hamilton Heights-Inwood Columbia Aging Project (WHI-CAP). *Alzheimer Dement.* **2020**, *16*, 1638−1649.

(13) Herbert, D.; Franz, S.; Popkova, Y.; Anderegg, U.; Schiller, J.; Schwede, K.; Lorz, A.; Simon, J. C.; Saalbach, A. High-Fat Diet Exacerbates Early Psoriatic Skin Inflammation Independent of Obesity: Saturated Fatty Acids as Key Players. *J. Invest. Dermatol.* **2018**, *138*, 1999−2009.

(14) Zhou, H.; Urso, C.; Jadeja, V. Saturated Fatty Acids in Obesity-Associated Inflammation. *J. Inflammation Res.* **2020**, *13*, 1−14.

(15) Jenkins, B.; West, J. A.; Koulman, A. A Review of Odd-Chain Fatty Acid Metabolism and the Role of Pentadecanoic Acid (C15:0) and Heptadecanoic Acid (C17:0) in Health and Disease. *Molecules* **2015**, *20*, 2425−2444.

(16) Kurotani, K.; Sato, M.; Yasuda, K.; Kashima, K.; Tanaka, S.; Hayashi, T.; Shirouchi, B.; Akter, S.; Kashino, I.; Hayabuchi, H.; Mizoue, T. Even- and odd-chain saturated fatty acids in serum phospholipids are differentially associated with adipokines. *PLoS One* **2017**, *12*, No. e0178192.

(17) Venn-Watson, S.; Lumpkin, R.; Dennis, E. A. Efficacy of dietary odd-chain saturated fatty acid pentadecanoic acid parallels broad associated health benefits in humans: could it be essential? *Sci. Rep.* **2020**, *10*, No. 8161.

(18) Wei, X.; Li, Y.; Zhou, S.; Guo, C.; Dong, X.; Li, Q.; Guo, J.; Wang, Y.; Huang, L. The Differences of Nutrient Components in Edible and Feeding Coix Seed at Different Developmental Stages Based on a Combined Analysis of Metabolomics. *Molecules* **2023**, *28* (9), 3759−3772.

(19) Guo, M.; Qu, D.; Qin, Y.; Chen, Y.; Liu, Y.; Huang, M.; Chen, Y. Transferrin-Functionalized Microemulsions Coloaded with Coix Seed Oil and Tripterine Deeply Penetrate To Improve Cervical Cancer Therapy. *Mol. Pharmaceutics* **2019**, *16*, 4826−4835.

(20) Fang, T.; Jiang, Y.-X.; Chen, L.; Huang, L.; Tian, X.-H.; Zhou, Y.-D.; Nagle, D. G.; Zhang, D.-D. Coix Seed Oil Exerts an Anti−Triple-Negative Breast Cancer Effect by Disrupting miR-205/S1PR1 Axis. *Front. Pharmacol.* **2020**, *11*, No. 529962.

(21) Dąbrowski, G.; Konopka, I. Update on food sources and biological activity of odd-chain, branched and cyclic fatty acids - A review. *Trends Food Sci. Technol.* **2022**, *119*, 514−529.

(22) Abdoul-Aziz, S. K. A.; Zhang, Y.; Wang, J. Milk Odd and Branched Chain Fatty Acids in Dairy Cows: A Review on Dietary Factors and Its Consequences on Human Health. *Animals* **2021**, *11*, 3210−3223.

(23) Bomfim, V. S.; Junior, A. A. J.; Alves, L. G.; Martinez, F. E.; Camelo, J. S., Jr. Human milk enriched with human milk lyophilisate for feeding very low birth weight preterm infants: A preclinical experimental study focusing on fatty acid profile. *PLoS One* **2018**, *13*, No. e0202794.

(24) Rawendra, R. D.; Lo, D.; Dikwatama, A. V. Comparative Study of Fatty Acid Composition and Sensory Acceptance of Indonesian Shortfin Eel (Anguilla bicolor) and Farmed Atlantic Salmon (Salmo salar). *IOP Conf. Ser.: Earth Environ. Sci.* **2021**, *794*, No. 012143.

(25) O'Brien, J. S.; Fillerup, D. L.; Mead, J. F. Brain lipids: I. Quantification and fatty acid composition of cerebroside sulfate in human cerebral gray and white matter. *J. Lipid Res.* **1964**, *5*, 109−116.

(26) Galvan-Miyoshi, J.; Ramos, S.; Ruiz-Garcia, J.; Castillo, R. Localized oscillations and Fraunhofer diffraction in crystalline phases of a monolayer. *J. Chem. Phys.* **2001**, *115*, 8178−8184.

(27) Ramos, S.; Castillo, R. Langmuir monolayers of C17, C19, and C21 fatty acids: Textures, phase transitions, and localized oscillations. *J. Chem. Phys.* **1999**, *110*, 7021−7030.

(28) Soler, F. J. P. Multiple reflections in an approximately parallel plate. *Opt. Commun.* **1997**, *139*, 165−169.

(29) Hénon, S.; Meunier, J. Microscope at the Brewster angle: Direct observation of first-order phase transitions in monolayers. *Rev. Sci. Instrum.* **1991**, *62*, 936−939.

(30) Teer, E.; Knobler, C. M.; Lautz, C.; Wurlitzer, S.; Kildae, J.; Fischer, T. M. Optical measurements of the phase diagrams of Langmuir monolayers of fatty acid, ester, and alcohol mixtures by Brewster-angle microscopy. *J. Chem. Phys.* **1997**, *106*, 1913−1920.

(31) Kaganer, V. M.; Möhwald, H.; Dutta, P. Structure and phase transitions in Langmuir monolayers. *Rev. Mod. Phys.* **1999**, *71*, 779−819.

(32) Xie, J.; Xu, G.; Wang, J.; Zhang, F.; Zhang, Y. Steady-State Motion Visual Evoked Potentials Produced by Oscillating Newton's Rings: Implications for Brain-Computer Interfaces. *PLoS One* **2012**, *7*, No. e39707.

(33) Zhang, R.-Q.; Lifshitz, Y.; Lee, S.-T. Oxide-Assisted Growth of Semiconducting Nanowires. *Adv. Mater.* **2003**, *15*, 635−640.

(34) Smith, R. D.; Berg, J. C. The collapse of surfactant monolayers at the air—water interface. *J. Colloid Interface Sci.* **1980**, *74*, 273−286.

(35) Sebinelli, H. G.; Borin, I. A.; Ciancaglini, P.; Bolean, M. Topographical and mechanical properties of liposome surfaces harboring Na,K-ATPase by means of atomic force microscopy. *Soft Matter* **2019**, *15*, 2737−2745.

(36) Karabasz, A.; Szuwarzyński, M.; Nowakowska, M.; Bzowska, M.; Lewandowska-Łańcucka, J. Stabilization of liposomes with silicone layer improves their elastomechanical properties while not compromising biological features. *Colloids Surf., B* **2020**, *195*, No. 111272.

(37) Liang, X.; Mao, G.; Ng, K. S. Probing small unilamellar EggPC vesicles on mica surface by atomic force microscopy. *Colloids Surf., B* **2004**, *34*, 41−51.

(38) Reviakine, I.; Brisson, A. Formation of Supported Phospholipid Bilayers from Unilamellar Vesicles Investigated by Atomic Force Microscopy. *Langmuir* **2000**, *16*, 1806−1815.

(39) Gopal, A.; Lee, K. Y. C. Morphology and Collapse Transitions in Binary Phospholipid Monolayers. *J. Phys. Chem. B* **2001**, *105*, 10348−10354.

(40) Phan, M. D.; Lee, J.; Shin, K. Collapsed States of Langmuir Monolayers. *J. Oleo Sci.* **2016**, *65*, 385−397.

(41) Ridsdale, R.; Palaniyar, N.; Possmayer, F.; Harauz, G. Formation of Folds and Vesicles by Dipalmitoylphosphatidylcholine Monolayers Spread in Excess. *J. Membr. Biol.* **2001**, *180*, 21−32.

(42) Hatta, E. Division and Fusion, Extension, Adhesion, and Retraction of Vesicles Created through Langmuir Monolayer Collapse: Cell-like Behavior. *J. Phys. Chem. B* **2007**, *111*, 10155−10159.

(43) Chi, L. F.; Anders, H. F. M.; Fuchs, H.; Johnston, R. R.; Ringsdorf, H. Domain Structures in Langmuir-Blodgett Films Investigated by Atomic Force Microscopy. *Science* **1993**, *259*, 213−216.

(44) Murthy, A. V. R.; Guyomarc'h, F.; Lopez, C. The temperature-dependent physical state of polar lipids and their miscibility impact the topography and mechanical properties of bilayer models of the milk fat globule membrane. *Biochim. Biophys. Acta, Biomembr.* **2016**, *1858*, 2181−2190.

(45) Wood, M. H.; Milan, D. C.; Nichols, R. J.; Casford, M. T. L.; Horswell, S. L. A quantitative determination of lipid bilayer deposition efficiency using AFM. *RSC Adv.* **2021**, *11*, 19768−19778.

(46) Menger, F. M. Laplace pressure inside micelles. *J. Phys. Chem.* **1979**, *83*, 893−893.

(47) Kirkham, M. C. Thermodynamics of the Elasticity of Natural Rubber. Ph.D. Thesis, The University of Manchester: United Kingdom, 1967.

(48) Kmetko, J.; Datta, A.; Evmenenko, G.; Dutta, P. The Effects of Divalent Ions on Langmuir Monolayer and Subphase Structure: A Grazing-Incidence Diffraction and Bragg Rod Study. *J. Phys. Chem. B* **2001**, *105*, 10818−10825.

(49) Has, C.; Sunthar, P. A comprehensive review on recent preparation techniques of liposomes. *J. Liposome Res.* **2020**, *30*, 336−365.

(50) Bañuelos-Frias, A.; Castañeda-Montiel, V. M.; Alvizo-Paez, E. R.; Vazquez-Martinez, E. A.; Gomez, E.; Ruiz-Garcia, J. Thermodynamic and Mechanical Properties of DMPC/Cholesterol Mixed Monolayers at Physiological Conditions. *Front. Phys.* **2021**, *9*, No. 636149.

(51) Sarkis, J.; Vié, V. Biomimetic Models to Investigate Membrane Biophysics Affecting Lipid−Protein Interaction. *Front. Bioeng. Biotechnol.* **2020**, *8*, No. 270.

(52) Langer, R. New Methods of Drug Delivery. *Science* **1990**, *249*, 1527−1533.

(53) Allen, T. M.; Cullis, P. R. Liposomal drug delivery systems: From concept to clinical applications. *Adv. Drug Delivery Rev.* **2013**, *65*, 36−48.